applied sciences

Article

Off-Axis Tension Behaviour of Unidirectional PEEK/AS4 Thermoplastic Composites

Yifan Ma [1], Yazhi Li [1,*] and Lu Liu [1,2]

[1] Department of Aeronautical Structural Engineering, School of Aeronautics, Northwestern Polytechnical University, Xi'an 710072, China
[2] Department of Aircraft Design, School of Aircraft, Xi'an Aeronautical University, Xi'an 710000, China
* Correspondence: yazhi.li@nwpu.edu.cn

Abstract: An experimental method for non-standard off-axis tension tests of unidirectional composites is developed. A new oblique end-tab is designed to eliminate stress concentration and in-plane bending moment induced by off-axis tension loading. Finite element analysis and experiments on Polyetheretherketone (PEEK)/AS4 unidirectional thermoplastic composites (CFRTP) were conducted to evaluate the effectiveness of the proposed testing method. Simulation and test results demonstrate that the use of oblique end-tabs eradicates stress concentration and bending movements. The digital image correlation (DIC) method was used to help investigate the full-field tension/shear coupling deformation response of the off-axis specimen. Test results show significant nonlinear behaviour and inhomogeneous strain distribution under tension/shear combined stresses. A fractographic study was carried out to study the damage mechanisms under a tension/shear combined stress state. Specimens with 30°, 45° and 60° off-axis angles, fail in tension/shear mixed failure mode. Fracture surface morphology indicates that matrix plastic deformation and ductile drawing under tension/shear coupled stress state induced the nonlinear stress-strain response.

Keywords: thermoplastic composites; off-axis tension; tension/shear coupling; digital image correlation; fractography

Citation: Ma, Y.; Li, Y.; Liu, L. Off-Axis Tension Behaviour of Unidirectional PEEK/AS4 Thermoplastic Composites. *Appl. Sci.* **2023**, *13*, 3476. https://doi.org/10.3390/app13063476

Academic Editor: Patrick A. Fairclough

Received: 11 February 2023
Revised: 28 February 2023
Accepted: 3 March 2023
Published: 9 March 2023

1. Introduction

Polymer composites have drawn a vast amount of interest in the aerospace and aeronautical industries. The main advantage of polymer composite over metals is the high strength/weight ratio. The development of polymer materials has provided a wide range of matrix choices [1–3]. These polymer composites can be elastomer composites, thermoset composites or thermoplastic composites. The newly developed carbon fibre reinforced thermoplastic composites (CFRTP) have a semi-crystalline thermoplastic matrix which increased the performance and moulding processes compared to thermoset composites. The thermoplastic polymer is in the form of linear chains that shows ductile mechanical behaviour. Sevenois et al. [4] evaluated the tension and compression behaviours of open hole glass/PA6 thermoplastic cross-ply and quasi-isotropic laminates. A prominent nonlinear response was reported. Fedulov et al. [5] use the finite element (FE) method to study the transverse tension failure behaviour of unidirectional carbon fibre reinforced PEEK thermoplastic composites. Simulation results show that the thermoplastic matrix around the fibre/matrix interface exhibits a strengthening effect due to plastic deformation. Holmes et al. [6] compared the deformation modes of twin-hole specimens of three woven thermoplastic composite systems: glass fibre/polypropylene (PP), self-reinforced PP, and glass fibre/polycarbonate (PC). The measured strain fields show that the induced shear strain has a load-transfer effect on the deformation of the specimen and results in a lower fibre direction strain level. Bergmann et al. [7] compared the mechanical behaviours of three woven thermoplastic composites under ±45° quasi-static and high strain-rate tensile loading conditions. Results show that the materials are strain-rate sensitive and exhibit nonlinear responses. Lee et al. [8] conducted 0°, 45° and 90° tension and compression tests on short fibre reinforced thermoplastic composites. Different failure mechanisms were observed as the loading direction varies. Tan and Falzon [9] conducted in-plane shear tests on an AS4/PEKK thermoplastic composite and reported nonlinear response and plastic deformation. The effect of high toughness thermoplastic matrix on the mechanical response and failure mechanisms of CFRTP requires additional investigation.

Several biaxial test methods of fibre reinforced polymer composites were developed including biaxial tension of cruciform specimens, tension/torsion of tube specimens, and in-plane tension/shear of off-axis specimens [10]. Vankan et al. [11] carried out biaxial loading tests on AS4D/PEKK-FC thermoplastic quasi-isotropic laminates by subjecting cruciform specimens to a biaxial test rig with a suspended horizontal loading axis. Specimen buckling under compression loading was reported. Strain concentrations along the −45° and 45° directions were recorded due to induced shear stress. Zhang et al. [12] investigated the mechanical behaviour of a 3D woven T700/TDE-86 composite using short beam shear specimens with three different off-axis angles. Failure modes were changed from yarn tensile and delamination failure, to interface debonding and yarn pull-out. Gan et al. [13] employed a modified Arcan fixture (MAF) to conduct tension/shear and compression/shear combined loading tests on E-glass/RP528 epoxy composites. Comparing the stress-strain curves shows that the specimens fail at much higher stress and strain under compression-shear mixed loading conditions. The use of MAF would cause specimen pinhole shear-out failure when the off-axis angle is smaller than 30°. Laux et al. [14] also employed the MAF to experimentally study the tension/shear and compression/shear behaviours of quasi-isotropic open-hole carbon/epoxy composites. The ply thickness effect was reported with thin ply specimens showing higher strength.

Generally, tensile loads are applied along one of the principal axes of unidirectional composite laminates to measure the fibre tension or transverse tension properties (Figure 1a). In the off-axis tension test, the tensile loading direction is neither parallel nor perpendicular to the fibres. Hence the stress states correspond to the materials' principal axes are tension and shear mixed (Figure 1b). The off-axis tension test of fibre reinforced composites can be used for the characterization of the mechanical behaviour under multiaxial stress states. Hu et al. [15] conducted on-axis and off-axis tension tests of a URETEK 5893 woven composite. Rectangular specimen and end-tab designs were selected. The DIC collected strain fields of 45° specimens show that maximum strain appears at the edge corner, due to the unbalanced off-axis stress state. Han et al. [16] studied the fracture behaviour of a moso bamboo veneer composite subjected to off-axis loadings. Dumbbell-shaped off-axis tension specimens were subjected to tensile loadings. The observed tension/shear coupling failure mechanisms include fibre bridging and plastic deformation. Cai et al. [17] studied the off-axis tension responses of woven glass/epoxy composites experimentally. Both specimens show a nonlinear stress-strain relationship. Degraded elastic moduli were reported as the off-axis angle increases. Zhai et al. [18] carried out off-axis tension tests on E-glass/PP composites. Matrix plastic deformation and cleavage were observed under off-axis loading. However, investigations on off-axis loading have reported in-plane rotation moment and stress concentration, due to rigid clamping force and anisotropic material properties [19]. Chang et al. [20] and Cron et al. [21] used the end-pinned fixture to eliminate stress concentration within composite off-axis tension specimens. Test results show higher shear strength and strain compared to clamped off-axis tension test. A drawback of this method is stress concentration in the pinhole area could lead to specimen bearing or buckling failure.

Some researchers use modified end-tabs to produce uniformly distributed stress states and eliminate bending in off-axis tension specimens. Tahir et al. [22] proposed a tab design which has the same length as the specimen to restrict the out-of-plane deformation during the off-axis tension test of fibrous composites. Marín et al. [23] conducted 10° off-axis tension tests on AS4/3501-6 thermoset composites, using three different clamping conditions: add sandpaper between gripping jaws and specimen, attach glass-epoxy end-tabs to specimen ends, and clamp specimen ends directly. A comparison of the test results shows that the most reliable method is to use end-tabs. Richards et al. [24] investigated the effect of aspect ratio on stress distribution by the finite element method. Stress results indicate non-uniform distribution along the width of the specimens. Increasing the specimen aspect ratio would relieve the stress fluctuation. Sun and Berreth [25] proposed a new oblique end-tab design manufactured using glass fibre-reinforced silicon rubber. Pierron and Vautrin [19] conducted 10° off-axis tests using both regular and oblique end tabs. Finite element analysis shows oblique end-tabs produce a uniform deformation field. Tension stress was also detected, and the tension/shear coupled effect needs further research. Zhang et al. [26] carried out off-axis tension tests on PVC coated fabrics using dog-bone specimens with regular end-tabs. Images taken during the test show significant transverse deformation due to the bending moment. Merzkirch and Foecke [27] conducted a 10° off-axis tension test on thermoset composites using rectangle glass fibre end-tabs. Testing results and DIC full-field strain analysis show a non-uniform axial and shear strain distribution. The tension/shear coupling effect brings error to the measured shear strength. Current research on the off-axis behaviours of composites is mainly focused on the pure shear response of 10° off-axis specimens. However, when a lamina is under off-axis loading, normal stresses would produce shear strains and shear stresses produce normal strains. This tension/shear coupled effect on the material mechanical behaviour and the relationship with different fibre misalignment angles still require thorough study. Although the damage initiation and failure of thermoset composites were well investigated, as demonstrated in the Second World-Wide Failure Exercise (WWFE-II) [28]. The development of appropriate failure theories for thermoplastic composites is insufficient due to the lack of experimental information on biaxial tests.

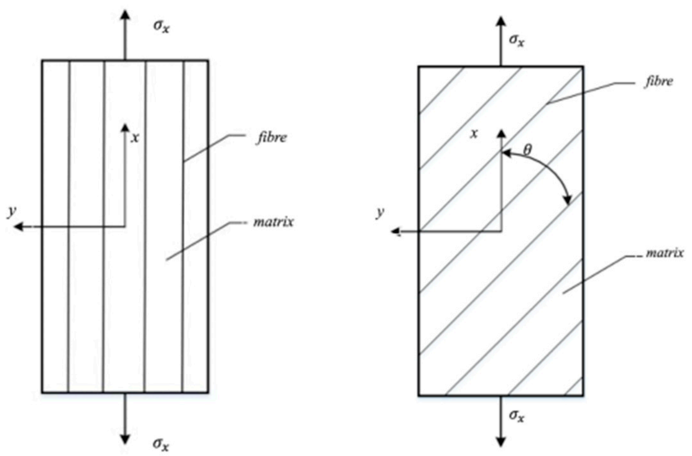

(a) (b)

Figure 1. Illustration of on-axis tension and off-axis tension tests: (**a**) On-axis tension test; (**b**) off-axis tension test.

The aim of this study is to (1) develop an oblique end-tab for off-axis tension tests, based on the mechanical properties of PEEK/AS4 thermoplastic composites, to eliminate stress concentration and in-plane bending moment; (2) conduct off-axis tension tests on unidirectional PEEK/AS4 thermoplastic laminates and, investigate the full field deformation and strain fields using the DIC method; (3) analyse the failure mechanisms and the tension/shear coupling effect under biaxial stress states based on DIC and SEM results.

2. Materials and Methods

The composite system used in this study is PEEK/AS4 thermoplastic epoxy/carbon Cetex® TC1200 prepreg produced by Toray Advanced Composites, Nottingham, UK. The nominal thickness of the prepreg is 0.14 mm. The AS4 carbon fibre has a diameter of 7 µm. The polyetheretherketone (PEEK) matrix is a high-performance engineering thermoplastic material. The density of the prepreg is 1.46 g/cm^3 and the resin content by weight is 34% in the lamina [29]. The basic properties of the PEEK/AS4 prepreg are summarized in Table 1.

Table 1. The properties of the PEEK/AS4 prepreg.

	PEEK/AS4
Matrix system	Polyetheretherketone (PEEK)
Fibre	AS4 carbon fibre
Fibre volume fraction	34%
Overall density	1.46 g/cm^3
Moulding	Hot press moulding
Thickness	0.14 mm

A 400 × 700 mm^2 unidirectional laminate was manually stacked and fabricated by hot pressing. The laminate was consolidated in the hot press compression chamber at 390 °C for 20 min and then cooled down at 4 °C/min until room temperature.

Off-axis tension specimens were cut at different orientations from the laminate by waterjet. Six off-axis angles θ = 15°, 30°, 45°, 60°, 75° and 90° (transverse compression) were selected to cover different combined stress states. The sketch of the off-axis tension specimen is shown in Figure 2. Nominal dimensions of the specimens were 120 mm (H) × 10 mm (W) × 3 mm (T). A slender specimen design is chosen with an aspect ratio of 12 to weaken the stress undulation across the width direction.

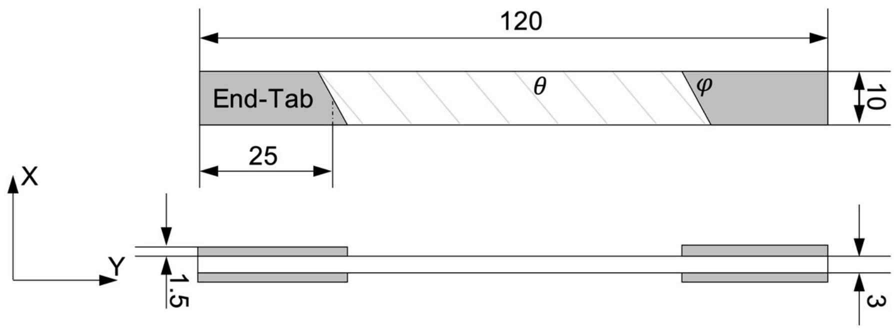

Figure 2. Off-axis tension specimen with oblique end-tabs.

2.1. End-Tab Design

Sun and Berreth [25] have proposed using oblique end-tabs in off-axis tension tests to counterbalance bending moment and eliminate stress concentration areas. The concept is to use a slant rigid connection between the loading point and the specimen to generate a uniformly distributed stress field. The end-tab oblique angle φ depends on the compliance of the off-axis lamina $\overline{S}_{ij}$:

$$cot\varphi = -\frac{\overline{S}_{16}}{\overline{S}_{11}} \quad (1)$$

For unidirectional laminate under plane-stress conditions, the off-axis compliance $\overline{S}_{ij}$ can be derived from the transformation of the on-axis compliance S_{ij}:

$$\begin{cases} \overline{S}_{11} = S_{11}cos^4\theta + (2S_{12} + S_{16})sin^2\theta cos^2\theta + S_{22}sin^4\theta \\ \overline{S}_{16} = (2S_{11} - 2S_{12} - S_{66})sin\theta cos^3\theta - (2S_{22} - 2S_{12} - S_{66})sin^3\theta cos\theta \end{cases} \quad (2)$$

The compliance coefficients can be expressed by material constants:

$$\begin{aligned} S_{11} &= \frac{1}{E_1} \\ S_{22} &= \frac{1}{E_2} \\ S_{66} &= \frac{1}{G_{12}} \\ S_{12} &= -\frac{-\nu_{21}}{E_1} \end{aligned} \tag{3}$$

Therefore, the corresponding oblique angles are calculated and listed in Table 2.

Table 2. End-tab oblique angle φ for different off-axis specimens.

Category	Angle				
Off-axis angle (°)	15	30	45	60	75
Oblique angle (°)	23	38	59	79	89

Oblique end-tabs are manufactured using glass fibre epoxy composite in the dimension of 25 mm × 10 mm. The nominal thickness of the end-tab is 1.5 mm.

The effect of this end-tab design on the failure mechanisms of thermoplastic composites is not analysed by any researcher. Hence finite element (FE) analysis and experimental investigation are carried out in this study.

A comparative study on rectangle and oblique end-tabs is carried out using the FE method. Three-Dimensional models of the specimen with two types of end-tabs were built in ABAQUS using an eight-node brick element with reduced integration (C3D8R). The properties of the thermoplastic composite lamina and end tab is listed in Table 3. A displacement loading of 0.2 mm was applied on the end-tab surfaces to simulate the experimental loading condition.

Table 3. Properties of PEEK/AS4 unidirectional lamina and glass fibre epoxy end-tab.

Category	PEEK/AS4						Glass Fibre Epoxy	
Property	E_1 (GPa)	E_2 (GPa)	G_{12} (GPa)	G_{23} (GPa)	υ_{12}	υ_{21}	E (GPa)	υ_{12}
Value	133	9.08	4.31	4.31	0.3	0.3	27.6	0.3

Representative deformation contour plots of 15° off-axis tension models are illustrated in Figure 3. Significant in-plane bending deformation was induced by the off-axis loading in the specimen with regular end-tabs. The oblique end-tab neutralized the bending moment and produced a uniform displacement field.

Figure 4a,b is the FE simulated stress contour plots of the 15° off-axis tension specimen. For the specimen with rectangle end-tabs, clear stress concentration points can be observed at the upper right and bottom left area of the specimen assessment area. The stress values are also not evenly distributed along the width direction. The application of oblique end-tabs eliminates stress concentration points, and the largest values are located along the hypotenuse of the end-tabs. The stresses are homogeneously distributed over the specimen length and width.

Figure 4c,d illustrates the simulated shear stress contour plots of the 15° off-axis tension specimen. A highly inhomogeneous shear stress field was generated in the specimen with rectangle end-tabs. Shear stress concentration points are located in the same corners as the axial stress field shows. The highest values are detected along the centre of the specimen width. The shear stresses of specimens with oblique end-tabs show uniform distribution.

FE analysis results have shown that the use of oblique end-tabs in a 15° off-axis tension specimen alleviates stress concentration and bending moment. Homogeneous strain fields are produced over the off-axis specimens with oblique end-tabs. The peak values of tensile and shear stresses of specimens with rectangle end-tabs are much higher than that of specimens using oblique tabs. The higher level of stress represents the earlier failure of the specimen with regular tabs during tests. Hence, by alternating the clamping condition using oblique end-tabs, a fully developed damage process and failure under tension/shear combined stresses can be obtained.

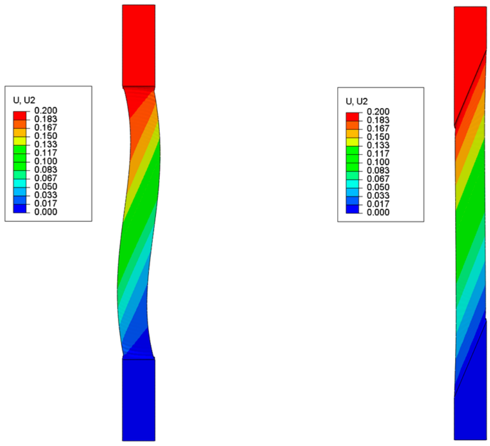

(**a**) (**b**)

Figure 3. Deformation plots of 15° off-axis tension specimens: (**a**) 15° off-axis tension specimen with rectangle end-tabs; (**b**) 15° off-axis tension specimen with oblique end-tabs.

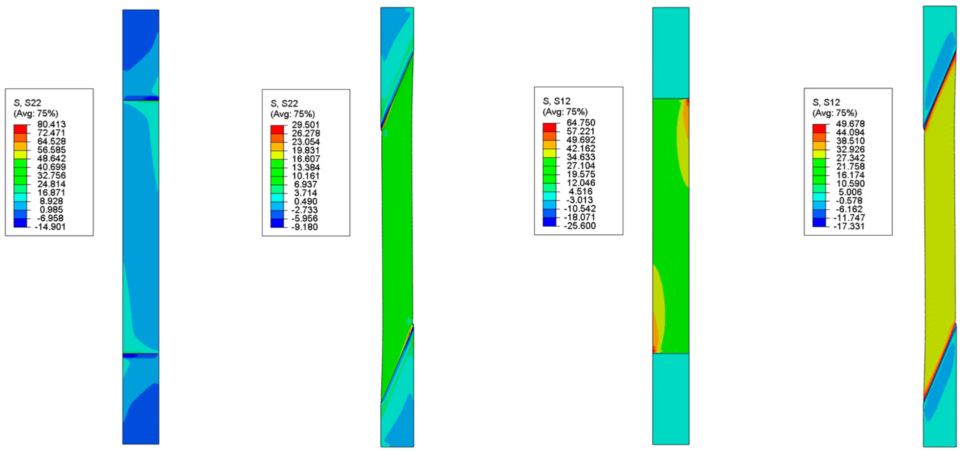

(**a**) (**b**) (**c**) (**d**)

Figure 4. Stress contour plots of 15° off-axis tension specimens: (**a**) σ_y of specimen with regular end-tabs; (**b**) σ_y of specimen with oblique end-tabs; (**c**) τ_{xy} of specimen with regular end-tabs; (**d**) τ_{xy} of specimen with oblique end-tabs.

2.2. DIC System

To apply the DIC measurement, all specimens were painted with matt white spray paint. When dried, black spray paint was carefully applied onto the surface to create a randomly distributed speckle pattern.

A GOM ARAMIS 4M 2D DIC system, manufactured by GOM in Braunschweig, Germany, is used to investigate the specimen deformation and strain variation during the tests. The system has a 4 Megapixel CMOS camera with a 35 mm lens. The image size was 2352 × 1728 pixels^2. Inspection of the speckle patterns using the DIC system is conducted to ensure the pattern density of approximately 50%. The measured average black pattern size is about 3.2 pixels. Images collected were analysed using the GOM ARAMIS 6.3.0 software provided by GOM mbH from Braunschweig, Germany to evaluate the displacement fields.

Suggestions were made by the iDICs [30] on the user-defined DIC parameters. According to the guide, the subset size should include at least three transitions from dark to white patterns and the step size ought to be 1/3 to 1/2 of the subset size. Hence, in this study, a subset size of 17 × 17 pixels^2 and a step size of 7 pixels were selected.

Engineering strain was calculated based on the virtual strain gauge (VSG) method. The strain computed using this method in the DIC analysis system is the average of all the strain data calculated within the pre-selected VSG region. The VSG size was set at 45 pixels in this work.

2.3. Off-Axis Tension Experiment

The off-axis tension tests were conducted on a DDL100 electronic universal testing machine manufactured by Sinotest Equipment Co., Ltd. in Changchun, China. A 100 kN load cell was used. The specimen was placed on the testing machine with both end-tabs fully clamped in the jaws. The loading rate is 0.5 mm/min. DIC system acquisition frequency was set at 1 Hz to capture all deformation stages.

3. Results and Discussion

3.1. Mechanical Response

Six groups of off-axis specimens were subjected to tension tests. Each group has six samples. Since all specimens fractured in the same mode, a representative 45° off-axis tension specimen, after failure, is selected and shown in Figure 5a. Final failure occurs with a matrix crack along the fibre direction for all tested specimens. The fracture surfaces are parallel to the $x - z$ plane. Figure 5b shows the oblique end-tab region after the 45° off-axis tension test. The clamping dents indicate no sliding or rotation during the test and therefore validates the effectiveness of the oblique end-tabs.

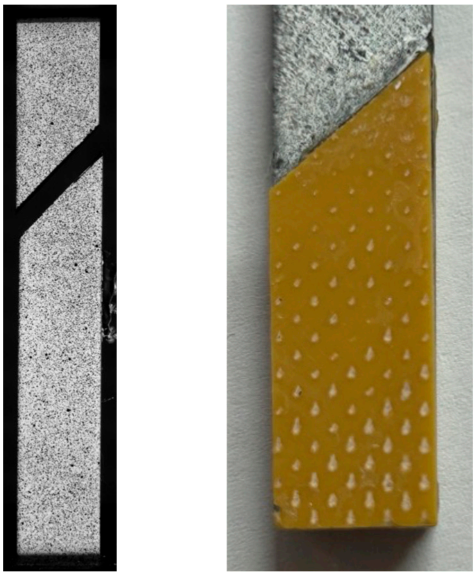

(**a**) (**b**)

Figure 5. Representative fractured 45° off-axis tension specimen: (**a**) Failure mode of a 45° off-axis tension specimen; (**b**) End-tab region of the specimen.

The extracted axial stress-strain curves are shown in Figure 6. All specimens exhibit significant nonlinear behaviour. The 15° off-axis tension specimen shows a linear stress-strain relationship before the stress increased to 250 MPa. As the stress mounts, the specimen shows a nonlinear response. The failure strength of the 15° off-axis tension specimen is prominently higher than the other specimens. An explanation is that when the fibre misalignment angle is smaller than 15°, fibre is the primary load bearing constituent, and the tension/shear coupling effect of the matrix is suppressed. Thus, the 15° off-axis specimen shows brittle behaviour with an elongation after fracture of 3%. When specimen off-axis angles are between 30°~60°, the stress-strain curves exhibit a linear relationship before the strain reaches 1%. The mechanical response then changed into a strain-hardening phase as the strain increases rapidly, and the stiffness decreased gradually until the final fracture. The 45° off-axis specimen has the largest failure strain of over 5%. Other than the brittle thermoset epoxy [17], the thermoplastic matrix demonstrates elastic-plastic behaviour. The 75° and 90° specimens have similar stress-strain relationships. The specimen elongation during the strain hardening stage is relatively short, indicating a decreased plastic deformation.

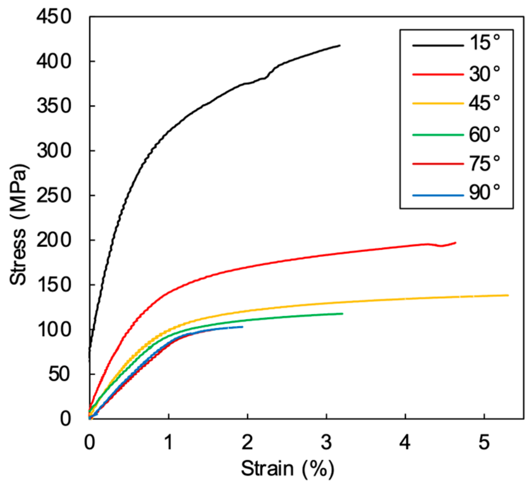

Figure 6. Stress-strain relationships of different off-axis tension tests.

The off-axis tension stiffness vs. off-axis angle relationship is shown in Figure 7a. The largest value of stiffness appears in the 15° off-axis specimen. The stiffness decreased sharply as the off-axis angle changed from 15° to 30°. The stiffness descent gently when the off-axis angle altered from 30° to 75°. The 75° and 90° specimens have nearly the same stiffness values. Figure 7b gives the off-axis tension strength vs the off-axis angle curve. The strength declines sharply from 419.6 MPa to 137.4 MPa with the angle increased from 15° to 45°. The strength then slowly descends to 102.1 MPa as the off-axis angle rises to 90°.

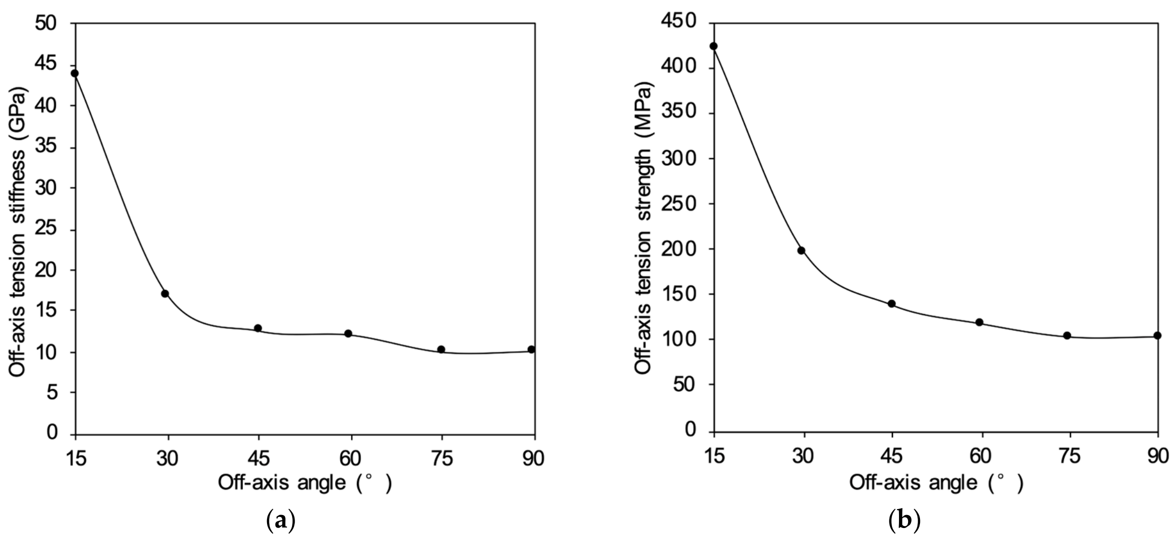

Figure 7. Relationships between material properties and off-axis angles: (**a**) Off-axis tension stiffness vs. off-axis angle curve; (**b**) Off-axis tension strength vs. off-axis angle curve.

The changing trends of strength and stiffness, with relation to off-axis angles, show that at a small off-axis angle of 15°, fibre is the main load-carrying component, and the material has maximum strength and stiffness. Loads transfer from fibre to matrix when, the off-axis angle increases to 30°, resulting in a rapid decrease in strength and stiffness. Tension and shear combined stress state forms and evolves as the off-axis angle changed from 30° to 90° but has fewer effects on the strength and stiffness values.

3.2. Full-Field Displacements and Strains Analysis

Full-field analysis of the displacements and strains is obtained based on the DIC technique and VSG method. DIC calculation, using subsets limits that the edges of the specimen and end-tabs, should be excluded.

Figure 8a,b depicts the representative displacement fields in the X and Y directions before the failure of the 15° off-axis tension specimens. The deformation in the Y direction is significantly higher than that in the X direction. The distribution of displacements has a high degree of uniformity. No distortion is generated along the width of the specimen compared to the report by Merzkirch and Foecke [27]. The strain fields show non-uniform distribution with scattered strain concentration points. The highest strain in the Y direction appears in the bottom left of the specimen and coincides with the final fracture location. The shear strain fields show homogeneous distribution. Few shear strain concentration points appear at the right edge of the specimen. The shear damage process of the matrix is affected by the coupled tensile stress, leading to discontinuously distributed strain fields. The displacement and strain fields of the 15° off-axis tension specimen, validate that by using oblique ted-tabs, the shear-induced in-plane bending moment is erased and a homogeneous stress state is ensured.

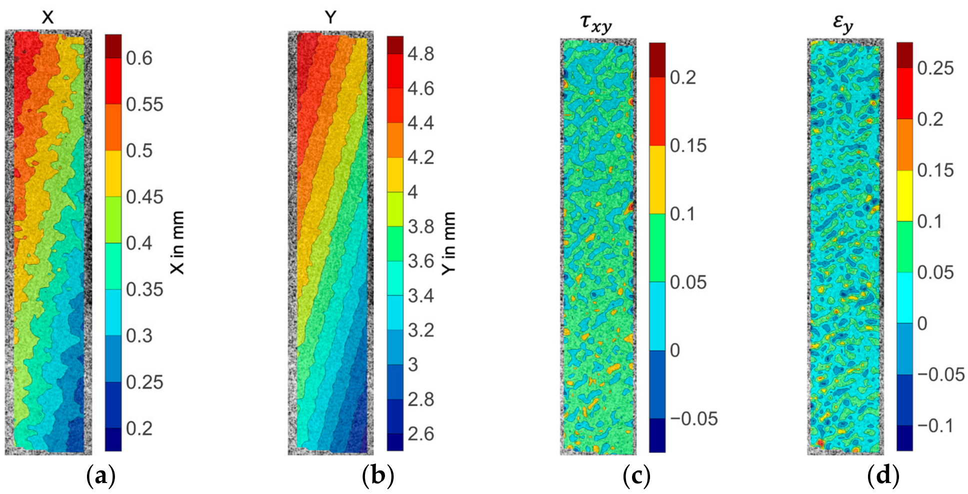

Figure 8. Representative DIC displacement and strain fields of 15° off-axis tension specimen: (**a**) X direction displacement field; (**b**) Y direction displacement field; (**c**) Shear strain field; (**d**) Tension strain field.

The displacement and strain fields of specimens with off-axis angles of 30°, 45° and 60° are alike. Therefore, a representative displacement and strain field of a 30° off-axis tension specimen is illustrated in Figure 9. The displacement fields have a uniform distribution along the fibre direction. The highest Y direction displacements emerge at the upper right corner of the specimen. The tension strain level is higher than that of the 15° off-axis tension specimen while the shear strain decreases. Both tension and shear strain fields show non-uniformity over the specimen, indicating mixed tension/shear stress states within the specimen [31]. The coupled stresses induced higher axial deformation compared to the 15° off-axis specimen. A comparison of the stress curves shows that the combined tension/shear stresses improve the damage and plastic deformation of the matrix.

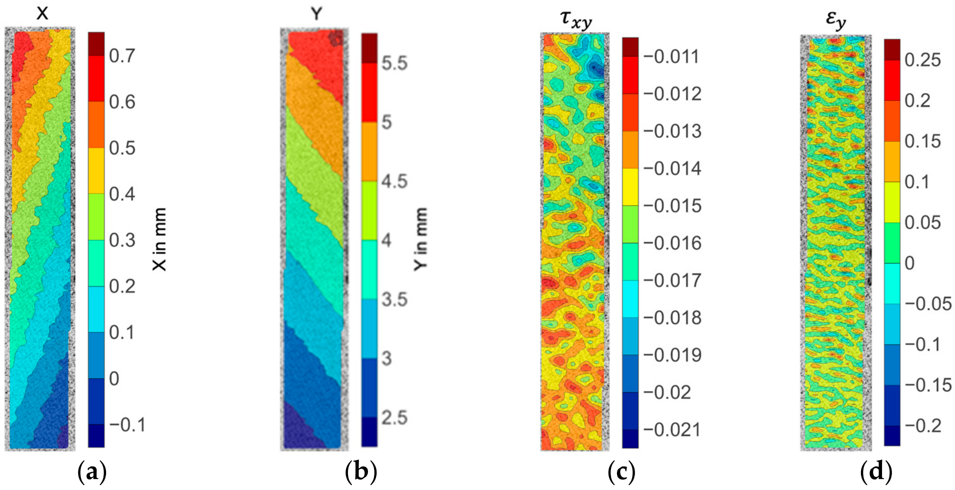

Figure 9. Representative DIC displacement and strain fields of 30° off-axis tension specimen: (**a**) X direction displacement fields; (**b**) Y direction displacement fields; (**c**) Shear strain field; (**d**) Tension strain field.

The 75° and 90° off-axis tension specimens have similar deformation patterns. A representative 75° off-axis tension specimen is chosen to analyse the deformation and strain behaviours. Figure 10 shows the displacement and strain fields of a 75° off-axis tension specimen. The displacements are evenly allocated through the specimen width. The highest displacement level is at the top of the specimen and gradually declines along the specimen length. The shear strain is significantly lower than the tension strain. The strain fields show regularity over the specimen width. Shear strain concentration points dispersed over the specimen surface. A tension strain concentration area is located at the right edge of the specimen but not coincident with the final failure position. The 75° and 90° off-axis specimens have the smallest deformation before failure, indicating that the matrix shows less ductility under pure tension stress.

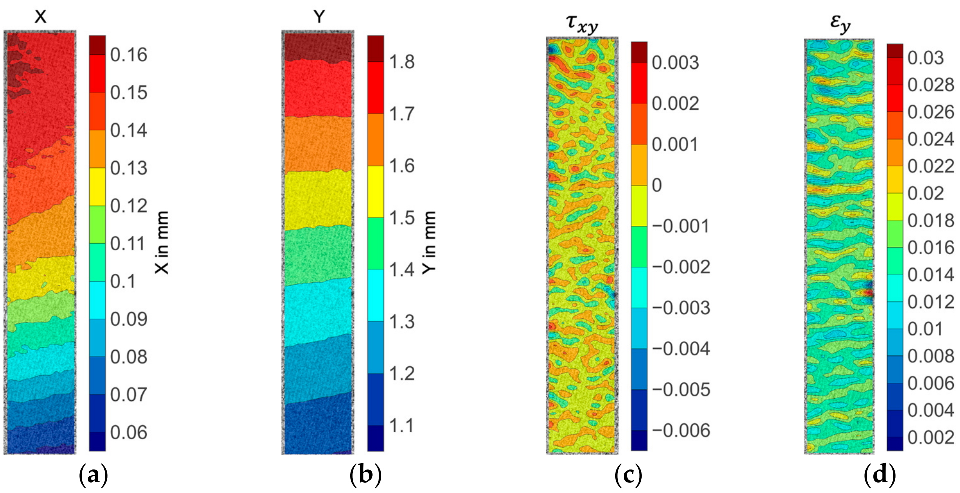

Figure 10. Representative DIC displacement and strain fields of 75° off-axis tension specimen: (**a**) X direction displacement fields; (**b**) Y direction displacement fields; (**c**) X direction strain fields; (**d**) Y direction strain fields.

3.3. Fractography

To further investigate the damage and failure mechanisms of the material under different combined stress states, the fractured surfaces were tested through the scanning electron microscope (SEM) method. Images were taken using a TESCAN VEGA II XMU scanning electron microscope (SEM) manufactured by TESCAN ORSAY HOLDING a.s., Brno-Kohoutovice, Czech Republic.

Figure 11a shows the fracture surface morphology of the 15° off-axis tension specimen. The shear stress dominated fracture surface is smooth and led to a small part of fibre fractures. The fibre surfaces are sleek due to fibre/matrix debonding under shear loading. The surface of the matrix reveals riverline, textured microflow and matrix plastic deformation features, implying the plastic behaviour of the matrix.

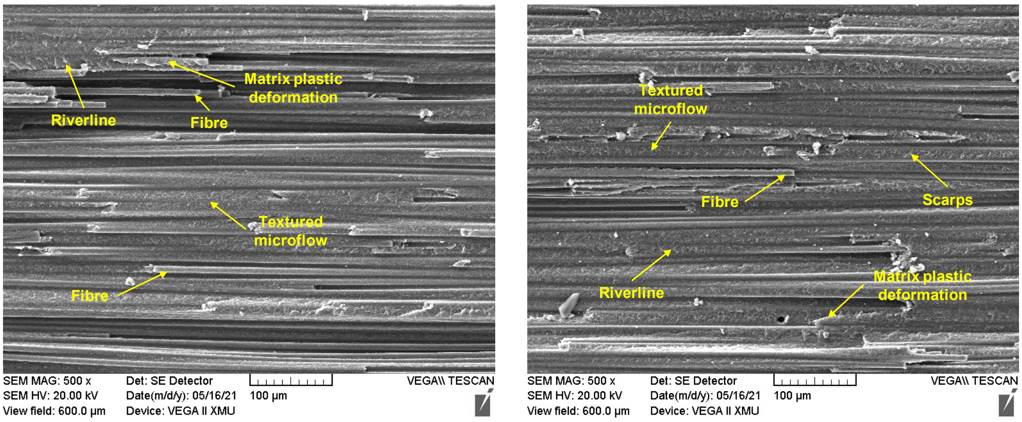

(**a**) (**b**)

Figure 11. Fracture surface morphology of different off-axis tension specimens: (**a**) 15°; (**b**) 30°.

Figure 11b is the SEM image of the fractured 30° off-axis tension specimen. As the off-axis angle increased, the tension stress component within the matrix increased. The fractured surface exhibits scarps, riverline and a larger amount of matrix plastic deformation under a tension/shear combined stress state. The tension/shear coupling effect leads to increased plastic fracture features. Fibre fractures can also be identified owing to tension loading.

Figure 12 compares the different fracture features of 45° and 60° off-axis specimens which have similar failure strengths. The increased tension stress generates a step-shaped feature on the fractured surface of the specimen with a 45° off-axis angle as shown in Figure 12a. Scarps features produced by tension/shear coupled stresses are all over the image. Matrix plastic deformation can also be spotted near the fibre surface.

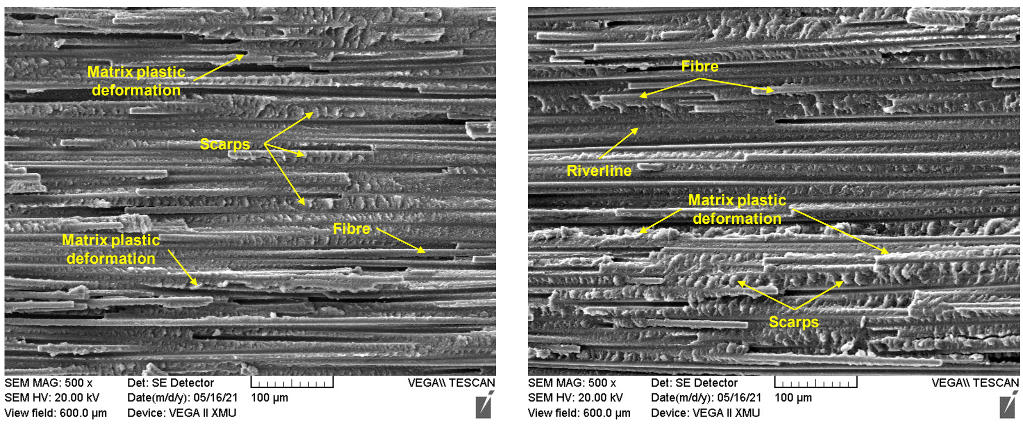

(**a**) (**b**)

Figure 12. Fracture surface morphology of different off-axis tension specimens: (**a**) 45°; (**b**) 60°.

An uneven fractured surface was created under 60° off-axis tension loading conditions as shown in Figure 12b. The size and distribution of the scarps feature on the matrix surface enlarged under decreased shear stress and inclined tension stress. The matrix around fibre surfaces developed plastic deformation features as a result of ductile fracture behaviour.

Figure 13 depicts the SEM images of the fractured 75° and 90° off-axis tension specimens. The surfaces of the failed specimens show similar patterns. Rough fractured surfaces are produced by matrix tension failure. The thermoplastic matrix exhibits ductile-brittle mixed fracture mode under tension. Some riverlines, after brittle fracture and plastic deformation, can be observed on the fractured surface of the polymer. The material shows a non-uniform fracture of the fibres due to resin-rich areas. The amount of fibre pull-out increases compared to the other off-axis specimens as a result of the effect of elevated tensile stress level.

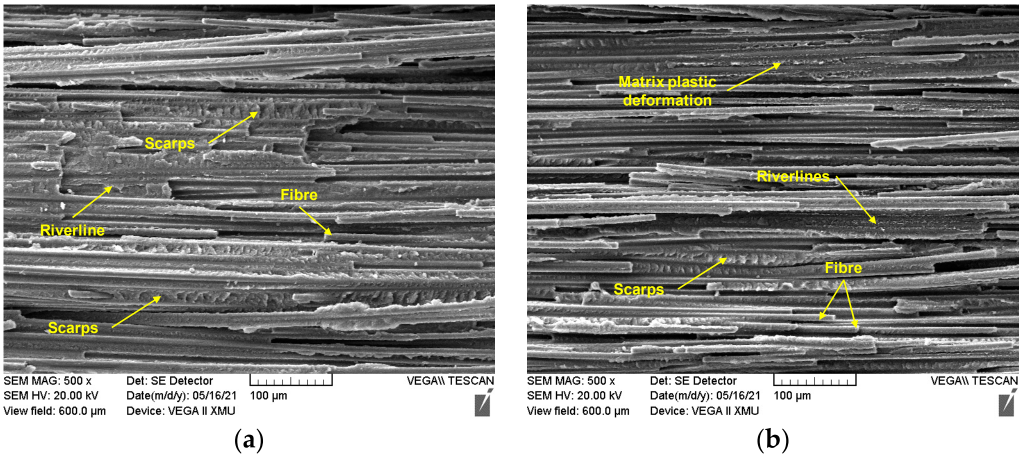

Figure 13. Fracture surface morphology of different off-axis tension specimens: (**a**) 75°; (**b**) 90°.

The fractographic study of the off-axis specimens shows that under a small off-axis angle of 15°, a high level of shear stress led to shear plastic damage of the matrix, and the fibres limited the material deformation. For specimens with off-axis angles of 30°, 45° and 60°, the tension and shear combined stresses promote the damage process in the matrix. The thermoplastic resin demonstrates ductile fracture behaviour under the tension/shear coupling effect. When the off-axis angle is larger than 75°, the composite shows a transverse tension failure character. The thermoplastic matrix shows ductile-brittle mixed fracture behaviour under tension stress.

4. Conclusions

This paper presents an experimental study on the unidirectional PEEK/AS4 thermoplastic composites, subjected to off-axis tension loads, using a full-field digital image correlation measurement technique. Conclusions are drawn as follows:

(1) Finite element simulation and experiments validate that, by using oblique end-tabs with angles designed according to the material properties, stress concentration and shear-induced bending moment could be eliminated.
(2) The mechanical response of the material exhibits a linear-elastic relationship at the first stage, and nonlinear behaviour at the strain-hardening stage. The combined tension and shear stress-induced tension/shear coupling effect promotes a higher level of nonlinearity and produces inhomogeneous strain fields. The strength and stiffness decline rapidly when the off-axis angle increases from 15° to 30°, and then decreases gradually.
(3) The primary failure mode for small off-axis angle specimens is matrix shear failure. The tension/shear coupling effect accelerates the damage process of the matrix resulting in tension/shear combined ductile fracture mode. Specimens with large off-axis angles exhibit matrix tension failure feature.

Author Contributions: Conceptualisation, Y.M., Y.L. and L.L.; methodology, Y.M. and L.L.; software, Y.M.; validation, Y.L.; formal analysis, L.L.; investigation, Y.M. and L.L.; resources, Y.L.; data curation, Y.M.; writing—original draft preparation, Y.M.; writing—review and editing, Y.L.; visualisation, L.L.; supervision, Y.L.; project administration, Y.L. All authors have read and agreed to the published version of the manuscript.

Funding: This research received no external funding.

Institutional Review Board Statement: Not applicable.

Informed Consent Statement: Not applicable.

Data Availability Statement: Data available in a publicly accessible repository.

Conflicts of Interest: The authors declare no conflict of interest.

References

1. Vijay Kumar, V.; Balaganesan, G.; Lee, J.K.; Neisiany, R.E.; Surendran, S.; Ramakrishna, S. A Review of Recent Advances in Nanoengineered Polymer Composites. *Polymers* **2019**, *11*, 644. [CrossRef]
2. Mohamed, M.; Naguib, H.; El-Ghazawy, R.; Shaker, N.; Amer, A.; Soliman, A.; Kandil, U. Surface Activation of Wood Plastic Composites (WPC) for Enhanced Adhesion with Epoxy Coating. *Mater. Perform. Charact.* **2019**, *8*, 20180034. [CrossRef]
3. Naguib, H.M.; Hou, G. Exploitation of Natural and Recycled Biomass Resources to Get Eco-Friendly Polymer. *J. Polym. Environ.* **2023**, *31*, 533–540. [CrossRef]
4. Sevenois, R.D.; Yang, X.; Verboven, E.; Kersemans, M.; Van Paepegem, W. Permanent Deformation and Stiffness Degradation of Open Hole Glass/PA6 UD Thermoplastic Composite in Tension and Compression. *Materials* **2021**, *14*, 2646. [CrossRef]
5. Fedulov, B.; Fedorenko, A.; Safonov, A.; Lomakin, E. Nonlinear Shear Behavior and Failure of Composite Materials under Plane Stress Conditions. *Acta Mech.* **2017**, *228*, 2033–2040. [CrossRef]
6. Holmes, J.; Vlandis, G.; Stachurski, Z.; Das, R.; Compston, P. Failure Behaviour in Woven Thermoplastic Composites Subjected to Various Deformation Modes. *Compos. Part Appl. Sci. Manuf.* **2021**, *146*, 106410. [CrossRef]
7. Bergmann, T.; Heimbs, S.; Maier, M. Mechanical Properties and Energy Absorption Capability of Woven Fabric Composites under $\pm 45^{\circ}$ Off-Axis Tension. *Compos. Struct.* **2015**, *125*, 362–373. [CrossRef]
8. Lee, J.; Lee, H.; Kim, N. Fiber Orientation and Strain Rate-Dependent Tensile and Compressive Behavior of Injection Molded Polyamide-6 Reinforced with 20% Short Carbon Fiber. *Polymers* **2023**, *15*, 738. [CrossRef]
9. Tan, W.; Falzon, B.G. Modelling the Nonlinear Behaviour and Fracture Process of AS4/PEKK Thermoplastic Composite under Shear Loading. *Compos. Sci. Technol.* **2016**, *126*, 60–77. [CrossRef]
10. Olsson, R. A Survey of Test Methods for Multiaxial and Out-of-Plane Strength of Composite Laminates. *Compos. Sci. Technol.* **2011**, *71*, 773–783. [CrossRef]
11. Vankan, W.J.; Tijs, B.H.; de Jong, G.J.; de Frel, H.C.; Singh, N.K. Strength of Notched and Un-Notched Thermoplastic Composite Laminate in Biaxial Tension and Compression. *J. Compos. Mater.* **2016**, *50*, 3477–3500. [CrossRef]
12. Zhang, D.; Liu, X.; Gu, Y.; Sun, M.; Yu, S.; Zhang, Y.; Qian, K. Effects of Off-Axis Angle on Shear Progressive Damage of 3D Woven Composites with X-Ray Micro-Computed Tomography. *Compos. Part Appl. Sci. Manuf.* **2018**, *115*, 311–320. [CrossRef]
13. Gan, K.W.; Laux, T.; Taher, S.T.; Dulieu-Barton, J.M.; Thomsen, O.T. A Novel Fixture for Determining the Tension/Compression-Shear Failure Envelope of Multidirectional Composite Laminates. *Compos. Struct.* **2018**, *184*, 662–673. [CrossRef]
14. Laux, T.; Gan, K.W.; Dulieu-Barton, J.M.; Thomsen, O.T. Ply Thickness and Fibre Orientation Effects in Multidirectional Composite Laminates Subjected to Combined Tension/Compression and Shear. *Compos. Part Appl. Sci. Manuf.* **2020**, *133*, 105864. [CrossRef]
15. Hu, J.; Gao, C.; He, S.; Chen, W.; Li, Y.; Zhao, B.; Shi, T.; Yang, D. Effects of On-Axis and off-Axis Tension on Uniaxial Mechanical Properties of Plain Woven Fabrics for Inflated Structures. *Compos. Struct.* **2017**, *171*, 92–99. [CrossRef]
16. Han, S.; Chen, F.; Li, H.; Wang, G. Effect of Off-Axis Angle on Tension Failures of Laminated Moso Bamboo-Poplar Veneer Composites: An in Situ Characterization. *Mater. Des.* **2021**, *212*, 110254. [CrossRef]
17. Cai, D.; Zhou, G.; Wang, X.; Li, C.; Deng, J. Experimental Investigation on Mechanical Properties of Unidirectional and Woven Fabric Glass/Epoxy Composites under off-Axis Tensile Loading. *Polym. Test.* **2017**, *58*, 142–152. [CrossRef]
18. Zhai, Z.; Jiang, B.; Drummer, D. Characterization of Nonlinear Response in Quasi-Unidirectional E-Glass Fabric Reinforced Polypropylene Composites under off-Axis Tensile Loading. *Polym. Test.* **2017**, *63*, 521–529. [CrossRef]
19. Pierron, F.; Vautrin, A. The 10 Off-Axis Tensile Test: A Critical Approach. *Compos. Sci. Technol.* **1996**, *56*, 483–488. [CrossRef]
20. Chang, B.-W.; Huang, P.-H.; Smith, D.G. A Pinned-End Fixture for Off-Axis Testing. *Exp. Tech.* **1984**, *8*, 28–30. [CrossRef]
21. Cron, S.M.; Palazotto, A.N.; Sandhu, R.S. The Improvement of End-Boundary Conditions for off-Axis Tension Specimen Use. *Exp. Mech.* **1988**, *28*, 14–19. [CrossRef]
22. Tahir, M.M.; Wang, W.-X.; Matsubara, T. A Novel Tab for Tensile Testing of Unidirectional Thermoplastic Composites. *J. Thermoplast. Compos. Mater.* **2019**, *32*, 37–51. [CrossRef]
23. Marín, J.C.; Cañas, J.; París, F.; Morton, J. Determination of G12 by Means of the Off-Axis Tension Test. Part II: A Self-Consistent Approach to the Application of Correction Factors. *Compos. Part Appl. Sci. Manuf.* **2002**, *33*, 101–111. [CrossRef]

24. Richards, G.L.; Airhart, T.P.; Ashton, J.E. Off-Axis Tensile Coupon Testing. *J. Compos. Mater.* **1969**, *3*, 586–589. [CrossRef]
25. Sun, C.T.; Berreth, S.P. A New End Tab Design for Off-Axis Tension Test of Composite Materials. *J. Compos. Mater.* **1988**, *22*, 766–779. [CrossRef]
26. Zhang, L.; Zhang, Y.; Zhao, Q.; Xu, J.; Xue, J. Shape Effect Analysis of the Mechanical Properties of PVC-Coated Fabrics under Off-Axis Tension. *Adv. Mater. Sci. Eng.* **2020**, *2020*, 9634120. [CrossRef]
27. Merzkirch, M.; Foecke, T. 10° Off-Axis Testing of CFRP Using DIC: A Study on Strength, Strain and Modulus. *Compos. Part B Eng.* **2020**, *196*, 108062. [CrossRef]
28. Christensen, R.M. The World Wide Failure Exercise II Examination of Results. *J. Reinf. Plast. Compos.* **2013**, *32*, 1668–1672. [CrossRef]
29. Toray Advanced Composites Toray Cetex®TC1200 Data Sheet. Available online: https://www.toraytac.com/media/7765d981-1f9f-472d-bf24-69a647412e38/Pr7gdw/TAC/Documents/Data_sheets/Thermoplastic/UD%20tapes,%20prepregs%20and%20laminates/Toray-Cetex-TC1200_PEEK_PDS.pdf (accessed on 4 February 2023).
30. International Digital Image Correlation Society; Jones, E.M.C.; Iadicola, M.A. A Good Practices Guide for Digital Image Correlation; 2018. Available online: https://www.idics.org/guide/DICGoodPracticesGuide_ElectronicVersion-V5g-181022.pdf (accessed on 6 February 2023). [CrossRef]
31. Kashani, M.H.; Hosseini, A.; Sassani, F.; Ko, F.K.; Milani, A.S. Understanding Different Types of Coupling in Mechanical Behavior of Woven Fabric Reinforcements: A Critical Review and Analysis. *Compos. Struct.* **2017**, *179*, 558–567. [CrossRef]